Inorganic Chemistry
ARTICLE
pubs.acs.org/IC

Characterization of a Tricationic Trigonal Bipyramidal Iron(IV) Cyanide Complex, with a Very High Reduction Potential, and Its Iron(II) and Iron(III) Congeners

Jason England,[†] Erik R. Farquhar,[†] Yisong Guo,[‡] Matthew A. Cranswick,[†] Kallol Ray,[†] Eckard Münck,[*,‡] and Lawrence Que, Jr.[*,†]

[†]Department of Chemistry and Center for Metals in Biocatalysis, University of Minnesota, Minneapolis, Minnesota 55455, United States
[‡]Department of Chemistry, Carnegie Mellon University, Pittsburgh, Pennsylvania 15213, United States

S Supporting Information

ABSTRACT: Currently, there are only a handful of synthetic $S = 2$ oxoiron(IV) complexes. These serve as models for the high-spin ($S = 2$) oxoiron(IV) species that have been postulated, and confirmed in several cases, as key intermediates in the catalytic cycles of a variety of nonheme oxygen activating enzymes. The trigonal bipyramidal complex $[Fe^{IV}(O)(TMG_3tren)]^{2+}$ (**1**) was both the first $S = 2$ oxoiron(IV) model complex to be generated in high yield and the first to be crystallographically characterized. In this study, we demonstrate that the TMG$_3$tren ligand is also capable of supporting a tricationic cyanoiron(IV) unit, $[Fe^{IV}(CN)(TMG_3tren)]^{3+}$ (**4**). This complex was generated by electrolytic oxidation of the high-spin ($S = 2$) iron(II) complex $[Fe^{II}(CN)(TMG_3tren)]^{+}$ (**2**), via the $S = 5/2$ complex $[Fe^{III}(CN)(TMG_3tren)]^{2+}$ (**3**), the progress of which was conveniently monitored by using UV−vis spectroscopy to follow the growth of bathochromically shifting ligand-to-metal charge transfer (LMCT) bands. A combination of X-ray absorption spectroscopy (XAS), Mössbauer and NMR spectroscopies was used to establish that **4** has a $S = 0$ iron(IV) center. Consistent with its diamagnetic iron(IV) ground state, extended X-ray absorption fine structure (EXAFS) analysis of **4** indicated a significant contraction of the iron-donor atom bond lengths, relative to those of the crystallographically characterized complexes **2** and **3**. Notably, **4** has an $Fe^{IV/III}$ reduction potential of ∼1.4 V vs $Fc^{+/o}$, the highest value yet observed for a monoiron complex. The relatively high stability of **4** ($t_{1/2}$ in CD_3CN solution containing 0.1 M KPF_6 at 25 °C ≈ 15 min), as reflected by its high-yield accumulation via slow bulk electrolysis and amenability to ^{13}C NMR at −40 °C, highlights the ability of the sterically protecting, highly basic peralkylguanidyl donors of the TMG$_3$tren ligand to support highly charged high-valent complexes.

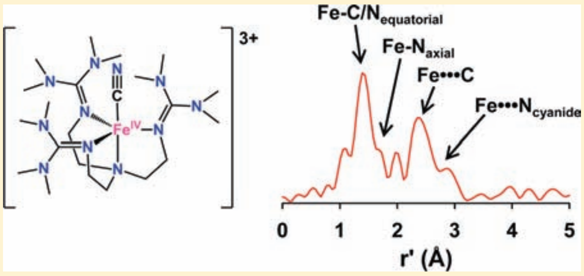

INTRODUCTION

Oxoiron(IV) intermediates have been invoked as the active oxidants in catalytic cycles of a wide variety of monoiron nonheme oxygenase enzymes[1,2] and have been trapped and spectroscopically characterized in several cases.[3−7] Without exception they were found to be high-spin ($S = 2$). In contrast, the overwhelming majority of the veritable plethora of model oxoiron(IV) complexes exhibit an $S = 1$ spin-state, supported within an octahedral ligand array.[8] Prior to our recent report of the generation and spectroscopic characterization of the trigonal bipyramidal (TBP) complex $[Fe^{IV}(O)(TMG_3tren)]^{2+}$ (**1**, Chart 1),[9] the only existing example of an $S = 2$ oxoiron(IV) complex was the purportedly octahedral $[Fe^{IV}(O)(H_2O)_5]^{2+}$.[10,11] It was subsequently demonstrated that **1** undergoes self-decay via intramolecular hydroxylation, as illustrated by a large KIE (24 at 25 °C) for the perdeuteromethyl isotopomer of TMG$_3$tren.[12] The increased stability conferred by deuteration was exploited to provide the X-ray structure of **1**, the first example of a crystallographically characterized high-spin oxoiron(IV) complex. Shortly thereafter, Borovik and co-workers reported the preparation, spectroscopic properties, and crystal structure of another $S = 2$ oxoiron(IV) complex, $[Fe^{IV}(O)(H_3buea)]^{-}$ (**5**), where H$_3$buea is the tetradentate tren-derived ligand $[(^{t}BuNHC(O)NCH_2CH_2)_3N]^{3-}$.[13] As a consequence of the trianionic nature of the H$_3$buea ligand, complex **5** exhibits a $Fe^{IV/III}$ redox couple at low potential (−0.90 V versus $[FeCp_2]^{+/0}$) and could be generated by ferrocenium oxidation of the corresponding iron(III) oxo or hydroxo complexes.

In addition to being a rare example of a synthetic high-spin oxoiron(IV) complex obtained in high yield, **1** was the second of only three published TBP complexes to possess both metal-atom multiple bonding and more than one d-electron,[14] with $[Mn^{IV}(O)(H_3buea)]^{-}$ being the first.[15] Though TBP imido- and oxoiron(IV) complexes have been invoked in several cases as highly reactive intermediates,[16−19] the only other report of a bona fide (confirmed by Mössbauer) TBP iron(IV) complex was

Received: October 15, 2010
Published: March 07, 2011

dx.doi.org/10.1021/ic102094d | *Inorg. Chem.* 2011, 50, 2885–2896

Chart 1

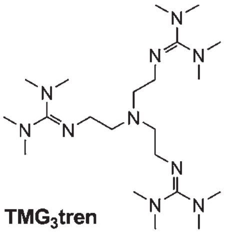

TMG$_3$tren

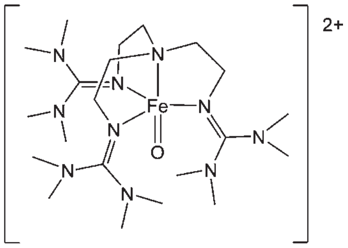

1

Chart 2

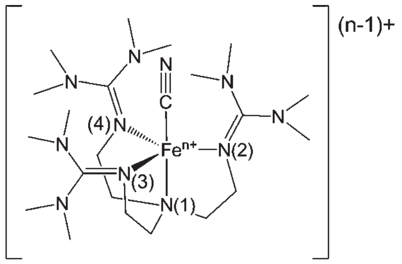

2: n = 2

3: n = 3

4: n = 4

that of the diamagnetic cyanide complex $[Fe^{IV}(CN)(N_3N')]$ (**6**), where $N_3N' = [(t\text{-}BuMe_2SiNCH_2CH_2)_3N]^{3-}$.[20] The $S = 0$ spin-state of **6** contrasts with the intermediate spin ($S = 1$) of the other existing iron(IV) cyanide complex $[Fe^{IV}(CN)(DCB)]^-$ (**7**), supported by a member of the macrocyclic tetraanionic TAML ligand family, which is believed to have a square-based pyramidal geometry.[21,22] Complex **6** was synthesized by oxidation of a trigonal pyramidal ferric precursor in the presence of cyanide, without isolation of the corresponding iron(III) cyanide complex, whereas **7** was prepared by metathesis of the chloride ligand in the crystallographically characterized $[Fe^{III}(Cl)(DCB^{+\bullet})]^-$.

A consequence of the deficit of high-spin oxoiron(IV) complexes is that there is very little context for interpretation of the spectroscopic data obtained for **1** and therefore a limited ability to assess the origin of any differences with enzymatic oxoiron(IV) intermediates. This problem is further exacerbated by there being few examples of iron complexes ligated by multidentate peralkylguanadinyl ligands and a limited number of iron(IV) complexes with a TBP geometry. Hence, we set out to elucidate trends in the electronic and spectroscopic properties of iron complexes of TMG$_3$tren as a function of oxidation state, within a static TBP ligand arrangement. Although such a systematic study was performed by Wieghardt and co-workers within an octahedral environment supported by pentadentate carboxymethylene-appended tetraazamacrocycles,[23−25] the oxidative innocence of TMG$_3$tren coupled with the strongly basic nature and ample steric protection afforded by peralkylguanidines provided a unique opportunity to access highly positively charged high-valent TBP iron complexes, by sequential one-electron oxidation of iron(II) starting materials. Given the precedence for a TBP iron(IV) cyanide complex,[20] we chose $[Fe^{II}(CN)(TMG_3tren)]^+$ (**2**) as a starting point for our studies. It was found that this complex could indeed be electrochemically oxidized to the corresponding iron(III) (**3**) and iron(IV) (**4**) cyanide complexes (Chart 2). Notably, the $Fe^{IV/III}$ reduction potential of ~1.4 V vs $Fc^{+/o}$ for **4** is the highest value yet observed for a monoiron complex. Here we report the structural characterization of **2** and **3** by X-ray crystallography and of **4** by X-ray absorption spectroscopy. The structural data and additional characterization by UV−vis, electron paramagnetic resonance (EPR), NMR, and Mössbauer spectroscopies show that **2** and **3** respectively have high-spin iron(II) and iron(III) centers, but **4** has a low-spin iron(IV) ($S = 0$) center.

EXPERIMENTAL SECTION

General Considerations. All reagents were purchased from commercial vendors and used as received, unless noted otherwise. Diethyl ether and tetrahydrofuran were dried by prolonged reflux, under a nitrogen atmosphere, over sodium metal with a benzophenone ketyl indicator and distilled freshly prior to use. Acetonitrile and dichloromethane were treated in a similar manner, but using calcium hydride as the drying agent. Ferrocenium triflate,[26] ferrocenium hexafluoroantimonate,[27] and the complex $[Fe^{II}(TMG_3tren)(OTf)](OTf)$ (**8**)[9] were prepared according to published procedures.

All moisture and oxygen sensitive compounds were prepared using standard high vacuum line, Schlenk, or cannula techniques. A nitrogen-filled glovebox was used for any subsequent manipulation and storage of these compounds. ^1H and ^{13}C NMR spectra were recorded on either Varian Inova 500 or 300 MHz spectrometers. Spectra were recorded in deuterated solvents, and chemical shifts (ppm) were referenced to residual protic solvent peaks. Elemental analyses were performed by Atlantic Microlab (Norcross, GA). Electronic spectroscopic measurements were performed using a HP8453A diode array spectrometer equipped with a cryostat from Unisoku Scientific Instruments (Osaka, Japan). Electrospray ionization mass spectrometry (ESI-MS) experiments were carried out on a Bruker BioTOF II mass spectrometer using a spray chamber voltage of 4000 V and a gas carrier temperature of 200 °C. FT-IR spectra were recorded in CH_3CN solution at ambient temperatures in a CaF_2 solution cell (International Crystal Laboratories), using an Avatar 370 spectrometer (ThermoNicolet).

Preparation of the Complexes. *$[Fe^{II}(CN)(TMG_3tren)]OTf$ (**[2]OTf**).* An equimolar quantity of **8** (0.40 g, 0.50 mmol) and NBu_4CN (0.14 g, 0.50 mmol) were dissolved in acetonitrile (5 mL) and stirred for 3 h. The resultant colorless solution was filtered, and the filtrate layered with diethyl ether (15 mL) and placed in a −35 °C freezer for 3 days. The crystalline material thereby obtained was isolated by filtration, washed with diethyl ether, and dried under vacuum to provide the product as an off-white solid (0.25 g, 74%). ^1H NMR (CD_3CN, all peaks appear as broad singlets): δ 174.4 (3H, CH_2), 104.8 (3H, CH_2), 46.5 (3H, CH_2), 33.3 (9H, NMe), 20.2 (9H, NMe), 11.3 (9H, NMe), 4.3 (9H, NMe). MS (+ESI): m/z 522.2 $[(\mathbf{2}\text{-}\mathbf{CN})^+]$. Anal. Calcd (found) for $C_{23}H_{48}F_3FeN_{11}O_3S$: C, 41.13 (41.41); H, 7.20 (7.38); N, 22.94 (23.11).

*[Fe^{II}(^{13}CN)(TMG$_3$tren)]OTf (**[2-^{13}CN]OTf**).* A mixture of **8** (0.40 g, 0.50 mmol) and $K^{13}CN$ (0.14 g, 0.50 mmol) was stirred for 12 h in acetonitrile (5 mL) and subsequently reduced to dryness. The resultant residue was extracted with dichloromethane (8 mL), filtered, and the filtrate layered with diethyl ether and placed at −35 °C for a few days. The colorless crystalline material that accumulated during this time was isolated by filtration, washed with diethyl ether, and dried under vacuum to give the product as a white solid (0.30 g, 89%). ^1H NMR (CD_3CN, all peaks appear as broad singlets): identical to [**2**]**OTf**. MS (+ESI): *m/z* 523.3 [(**2-^{13}CN**)$^+$]. Anal. Calcd (found) for $C_{22}{}^{13}CH_{48}F_3FeN_{11}O_3S$: C + ^{13}C as C, 41.13 (40.83); H, 7.19 (7.28); N, 22.91 (22.89).

X-ray Crystallography. Diffraction quality crystals of [**2**]**OTf** were grown by vapor diffusion of diethyl ether into concentrated CH_3CN solutions of complex. In contrast, crystals of **3** suitable for X-ray analysis were grown at −35 °C by layering concentrated solutions, produced by reaction of cold CH_3CN solutions of **2** with equimolar ferrocenium hexafluoroantimonate, with diethyl ether. Selected single crystals were placed onto the top of 0.1 mm diameter glass capillaries and mounted on a Bruker SMART V5.054 CCD area detector diffractometer for data collection. A preliminary set of cell constants was collected from reflections harvested from three sets of 20 frames. These initial sets of frames were oriented such that orthogonal wedges of reciprocal space were surveyed and then used to produce initial orientation matrices. Data collection was carried out using MoKα radiation (graphite monochromator). A randomly oriented region of reciprocal space was surveyed to the extent of one sphere and to a resolution of 0.77 Å, with four major sections of frames being collected using 0.30° steps in ω at four different ϕ settings and a detector position of −28° in 2θ. The intensity data were corrected for absorption and decay (SADABS).[28] Final cell constants were calculated from the actual data collection after integration (SAINT).[29] Please refer to Supporting Information, Tables S1 and S2, plus accompanying text, for additional crystal and refinement information.

The structures were solved and refined using Bruker SHELXTL.[30] Space groups were determined based on systematic absences and intensity statistics. In both cases a direct-methods solution was calculated, which provided most non-hydrogen atoms from the E-map. The remaining non-hydrogen atoms were located by full-matrix least-squares/difference Fourier cycles. All non-hydrogen atoms were refined with anisotropic displacement parameters. All hydrogen atoms were placed in ideal positions and refined as riding atoms with relative isotropic displacement parameters.

Electrochemistry. All electrochemical experiments were performed using either a BAS100B/W or a Cypress Systems CS-1200 computer-controlled potentiostat electroanalytical system, under air, at −40 °C, in either CH_3CN or CD_3CN solution, using 0.1 M supporting electrolyte and a standard three electrode setup. All potentials were referenced against the ferrocenium/ferrocene (Fc^+/Fc) couple. For low temperature cylic voltammetric experiments this three-electrode setup encompassed a glassy carbon working electrode (WE), Pt wire auxiliary electrode (AUX) and a Ag/Ag^+ reference electrode (REF). The latter was prepared by inserting a Ag wire into a 0.1 M CD_3CN solution of $AgNO_3$ contained within a glass tubing capped with a porous vycor tip and heat shrink tubing (BASi, Inc., West Lafayette, IN, U.S.A., part no. MF-2064). When not in use, this REF was stored in a vial containing a 0.1 M CD_3CN solution of NBu_4PF_6. Temperature of measurement was maintained using an ethanol/liquid nitrogen bath.

Controlled potential bulk electrolysis experiments were performed at −40 °C in a 1 cm rectangular UV−vis cuvette, using a WE composed of a cube of 100 ppi porous reticulated vitreous carbon (RVC) attached to a Pt wire, a heavily coiled Ag wire AUX and a Ag/Ag^+ REF. The latter two electrodes were housed in glass tubes, capped with porous vycor tips and heat shrink tubing, containing a CD_3CN solution of both 0.1 KPF_6 and 0.1 M $AgPF_6$. When not in use, these two electrodes were stored in a 0.1 M CD_3CN solution of KPF_6. The progress of all bulk electrolysis experiments were monitored via UV−vis, and the static potentials used in the oxidation of the **2** to **3** and **3** to **4** were +400 and +2000 mV, respectively. High-potential generation of **4** from **2** was performed in a stepwise fashion, via controlled low potential formation of **3**.

Resonance Raman Spectroscopy. Resonance Raman spectra were collected using Spectra-Physics Model 2060 krypton ion and 2030-15 argon ion lasers and an ACTON AM-506 monochromator equipped with a Princeton LN/CCD data collection system. Low temperature spectra in CH_3CN or CD_3CN were obtained at 77 K using a 135° backscattering geometry. Samples were frozen onto a gold-plated copper coldfinger in thermal contact with a Dewar flask containing liquid nitrogen. Raman frequencies were calibrated to indene prior to data collection. The monochromator slit width was set for a band-pass of 4 cm^{-1} for all spectra. The iron(III) spectra were collected using a laser excitation power of 100 mW, whereas the iron(IV) data was collected using an excitation power of 40−60 mW. The plotted spectra are an average of 32 scans with collection times of 30 s. All spectra were intensity corrected to the 710 or 773 cm^{-1} solvent peak of CD_3CN and CH_3CN, respectively.

X-ray Absorption Spectroscopy. *Sample Preparation.* All X-ray absorption spectroscopy (XAS) samples, with the exception of **2**, were generated electrolytically at −40 °C with 0.1 M NBu_4BF_4 supporting electrolyte using the procedures outlined above. Samples of **2** were prepared, with concentrations >18 mM, simply by dissolution in CH_3CN. Samples of **3** were generated in >90% yield, according to electronic spectroscopy, via bulk electrolysis of about 5 mM CH_3CN solutions of **2**. In contrast, samples of **4** were prepared by bulk electrolysis of approximately 3 mM CD_3CN solutions of 33% ^{57}Fe-enriched **2**, with Mössbauer spectroscopy demonstrating yields of ∼90%.

Data Collection. X-ray absorption data for **2**, **3**, and **4** were collected on beamline 7−3 of the Stanford Synchrotron Radiation Lightsource (SSRL) of SLAC National Accelerator Laboratory with storage ring conditions of 3.0 GeV and 80−100 mA. Fe K-edge XAS data were collected for frozen solutions maintained at a temperature of about 10−15 K over an energy range of 6.9−8.0 keV using a Si(220) double crystal monochromator for energy selection and an Oxford Instruments CF1208 continuous flow liquid helium cryostat for temperature control. Harmonic rejection was achieved by a 9 keV cutoff filter. Data was obtained as fluorescence excitation spectra with a 30 element solid-state germanium detector array (Canberra). An iron foil spectrum was recorded concomitantly for internal energy calibration, and the first inflection point of the K-edge was assigned to 7112.0 eV. The edge energies were routinely monitored during data collection for red-shifts indicative of sample photoreduction, but no experimentally significant photoreduction was observed for samples studied here.

Data Analysis. Data reduction, averaging, and normalization were performed using the program EXAFSPAK.[31] Following calibration and averaging of the data, background absorption was removed by fitting a Gaussian function to the pre-edge region and then subtracting this function from the entire spectrum. A three-segment spline with fourth order components was then fit to the EXAFS region of the spectrum to extract $\chi(k)$. The program pySpline was used to identify optimal parameters for the spline function employed in EXAFSPAK.[32] Analysis of the pre-edge features was carried out with the program SSExafs[33] using a previously described protocol.[34] The pre-edge fitting parameters reported are those providing the best match to both the experimental data and its second derivative.

Theoretical phase and amplitude parameters for a given absorber-scatterer pair were calculated using FEFF 8.40[35] and were utilized by the opt program of the EXAFSPAK package during curve-fitting. Parameters for **2** were calculated using the coordinates of the crystal structure without further modification. Parameters for **3** were calculated for a modification of the structure of **2** in which Fe−N$_{eq}$ and Fe−C$_{C\equiv N}$ were shortened to 2.00 Å, and Fe−N$_{ax}$ was shortened to 2.25 Å. Parameters for **4** were calculated for a further modification for the foregoing structure in which Fe−N$_{eq}$ and Fe−C$_{C\equiv N}$ were shortened to 1.80 Å, and Fe−N$_{ax}$ was shortened to 2.00 Å. The Fe−C≡N bond angle of 179.5° and the C≡N distance of 1.15 Å in **2** were assumed to be invariant in our EXAFS models of **3** and **4**. Phase and amplitude parameters for multiple-scattering pathways involving the Fe−C≡N moiety were explicitly calculated and employed in our EXAFS analyses. A number of possible multiple-scattering pathways involving the TMG$_3$tren ligand atoms were also considered, but were not deemed to contribute significantly to the observed EXAFS, as noted previously in our EXAFS analyses of **1** and its self-decay product.[9,12] In all analyses, the coordination number of a given shell was a fixed parameter, and was varied iteratively while bond lengths (r) and Debye−Waller factors (σ^2) were allowed to freely float. The amplitude reduction factor S_0 was fixed at 0.9. E_0, the point where $k = 0$ Å^{-1}, was taken to be 7122.25 eV for **2**, 7124.40 eV for **3**, and 7126.84 eV for **4**, and the edge shift parameter ΔE_0 was allowed to float as a single value for all shells in fits of a given complex. Therefore, in any given fit, the number of floating parameters was typically equal to (2 × num shells) + 1. The goodness of fit F was defined simply as $\Sigma(\chi_{exptl} - \chi_{calc})^2$. For fits to unfiltered data, a second goodness of fit parameter, F-factor, was defined as $[\Sigma k^6(\chi_{exptl} - \chi_{calc})^2/\Sigma k^6 \chi_{exptl}{}^2]^{1/2}$. To account for the effect that additional shells have on improving fit quality, an third goodness-of-fit metric F' was employed. $F' = F^2/(N_{IDP} - N_{VAR})$, where N_{VAR} is the number of floated variables in the fit, while N_{IDP} is the number of independent data points and is defined as $N_{IDP} = 2\Delta k \Delta r/\pi$.[36] In the latter equation, Δk is the k-range over which the data is fit, while Δr is the back-transformation range employed in fitting Fourier-filtered data. F' is thus of principal utility in fitting Fourier-filtered data, but can also be employed for unfiltered data by assuming a large value of Δr.

EPR and Mössbauer Spectroscopy. All EPR and Mössbauer samples were generated electrolytically at −40 °C, with 0.1 M NBu$_4$BF$_4$ supporting electrolyte, using the procedures outlined above. Mössbauer spectra were recorded using a Janis Research Super-Varitemp dewar that allowed studies in applied magnetic fields up to 8.0 T in the temperature range 1.5 to 200 K. Spectral simulations were performed using the WMOSS software package (SEE Co., Edina, MN). Isomer shifts are quoted relative to iron metal at 298 K. Perpendicular-mode X-band (9.62 GHz) EPR spectra were recorded on a Bruker EPR 300 spectrometer equipped with an Oxford ESR 910 liquid helium cryostat and an Oxford temperature controller. The microwave frequency was calibrated with a frequency counter and the magnetic field with a NMR gaussmeter. EPR simulations were carried out with a Windows software package (SpinCount) available from Professor M. P. Hendrich of Carnegie Mellon University.

RESULTS AND DISCUSSION

Synthesis and Characterization of Iron(II) Complexes. The iron(II) complex [Fe^{II}(TMG$_3$tren)(CN)](OTf) ([**2**](OTf)) was generated in a straightforward manner by metathesis of the solvent ligand in [Fe^{II}(TMG$_3$tren)(CH$_3$CN)](OTf)$_2$ (**8**), using either tetrabutylammonium or potassium cyanide salts. Consistent with its $S = 2$ ground state, established using the Evans' method ($\mu_B = 5.19\ \mu_B$),[37,38] the ^{1}H NMR spectrum of complex **2** exhibits well-defined paramagnetically shifted resonances distinct from those of the high-spin starting complex **8** (Supporting Information, Figure S1). The spectrum is indicative of a C_3-symmetric structure in which the three arms of the tripodal ligand are magnetically equivalent, on the NMR time scale, and the tetramethylguanidyl donors are canted with respect to one another, such that separate resonances are observed for the 4 methyl groups and 4 methylene protons of each ligand arm. This pseudo C_3-symmetry was retained in the solid-state, with the X-ray structure of [**2**](OTf) revealing an iron center with strictly TBP geometry (Figure 1, Table 1), which is reflected by a τ-value of 1.05.[39] (This unusually large τ-value is presumably a consequence

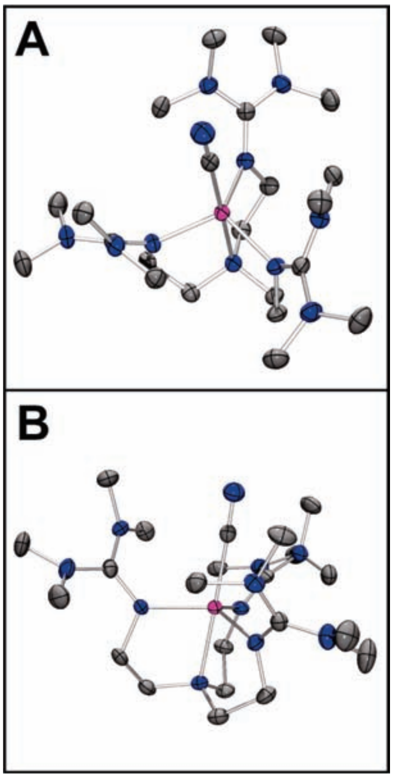

Figure 1. Thermal ellipsoid drawings of (**A**) **2** and (**B**) **3**, showing 50% probability ellipsoids. Hydrogen atoms, counterions, and solvent molecules have been omitted for clarity. Atom color scheme: C, gray; Fe, magenta; N, blue.

Table 1. Selected Bond Lengths (Å) and Angles (deg) for Complexes 2 and 3[a]

selected bond lengths (Å) and angles (deg)	2	3
Fe−CN	2.1293(15)	2.094(4)
Fe−N(1)	2.3017(12)	2.214(3)
Fe−N(2)	2.1138(12)	2.014(3)
Fe−N(3)	2.1160(12)	2.006(3)
Fe−N(4)	2.0992(12)	2.022(3)
C≡N	1.150(2)	1.144(4)
X−Fe−N(1)	179.52(5)	178.56(12)
X−Fe−N(2)	101.75(5)	100.11(13)
X−Fe−N(3)	102.50(5)	100.25(13)
X−Fe−N(4)	101.08(5)	98.32(12)
N(1)−Fe−N(2)	78.16(5)	80.26(11)
N(1)−Fe−N(3)	77.95(5)	80.77(11)
N(1)−Fe−N(4)	78.56(5)	80.30(11)
N(2)−Fe−N(3)	115.91(5)	117.15(12)
N(2)−Fe−N(4)	116.24(5)	118.35(12)
N(3)−Fe−N(4)	115.69(5)	116.40(12)

[a] See Chart 2 for atom labeling scheme.

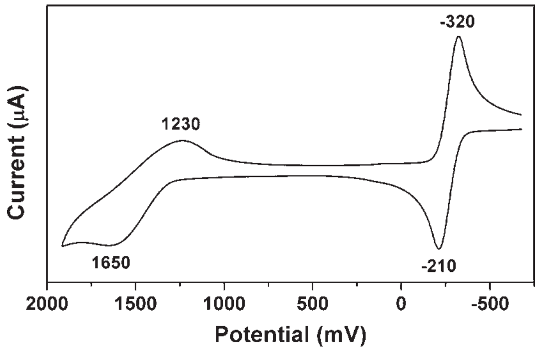

Figure 2. Cyclic voltammetric trace of **2** recorded in CD_3CN solution at −40 °C, using 0.1 M NBu_4PF_6 as supporting electrolyte. Potentials are plotted versus the Fc^+/Fc couple. Scan rate = 100 mV s^{-1}.

of the relatively large 0.431 Å displacement of the iron center away from the equatorial plane defined by the guanidine donors, toward the cyanide ligand.) A consistent atom labeling scheme was used for the X-ray structures detailed in this study and is outlined for the atoms directly coordinated to the metal center in Chart 2.

Complex **2** was found to exhibit Fe-donor atom bond distances typical of similarly ligated TBP high-spin iron(II) complexes.[9,17,40−43] As previously noted in other TMG_3tren complexes of iron,[9,12,40] the Fe−N(1) (2.3017(12) Å) bond is elongated relative to the average $Fe-N_{guanidine}$ distance (2.1097 Å), presumably because of the inherent strain resulting from the small bite angles ($\angle N(1)-Fe-N_{guanidine} \approx 78°$) associated with the three conjoined 5-membered chelate rings formed by its coordination. Further points of interest are the linearity of the $Fe-C\equiv N$ bond ($\angle Fe-C-N = 179.53°$) and the relatively short $C\equiv N$ bond length in **2-CN** of 1.150(2) Å (cf. the corresponding distance in NaCN is 1.18 Å).[44]

Cyclic Voltammetry. The room temperature cyclic voltammetric trace of **2** exhibits what is presumably a reversible Fe^{III}/Fe^{II} redox couple and some indication of a further oxidative process at much higher potential (Supporting Information, Figure S2). The latter is accompanied by a cathodic wave, but it is very broad and there is an additional reductive process at about 160 mV, which suggests that the product of high potential oxidation is prone to self-decay. In an attempt to stabilize any highly oxidized species formed, the measurements were repeated at −40 °C (Figure 2 and Table 2). Though low temperature did not significantly perturb the putative $Fe^{III/II}$ couple centered at −270 mV, the high potential anodic wave became better defined, and there was no indication of accompanying chemical decay (i.e., no anodic feature at 160 mV). The observed peak separation (ΔE) of approximately 400 mV between the anodic and the cathodic waves of this redox couple is relatively large, and this couple does not display behavior approaching that of a simple electron transfer process even at high scan rates (Supporting Information, Figure S3), which suggests that the large ΔE is not a consequence of chemical irreversibility, but likely reflects a significant kinetic barrier to electron transfer because of changes in iron spin state and structure accompanying this process (see below). Phenomena of this type have been previously reported,[45,46] and might be expected to kinetically stabilize this two-electron oxidized species. It should be noted that the high potential of the $E_{1/2} \approx 1400$ mV redox couple is at the upper limit of published iron-centered reduction potentials,[46] in accordance with formation of a highly positively charged iron(IV) species. However, ascribing these electrochemical features to the iron centered $Fe^{III/II}$ and $Fe^{IV/III}$ redox couples, respectively, requires rigorous spectroscopic oxidation state assignments (see below).

Chemical Generation of 3. As the putative $Fe^{III/II}$ redox couple observed for **2** is at low potential (−270 mV), its one-electron oxidized analogue should be readily chemically accessible. Indeed, it was found that addition of 1 equiv of ferrocenium ion to colorless solutions of **2** led to formation of an intensely red-brown colored species **3**, whose electrospray mass spectrum (Supporting Information, Figures S4 and S5) exhibited peaks at $m/z = 671.3$ and 261.2, with isotope distribution patterns consistent with their formulation as the ion fragments $\{[Fe^{III}(CN)(TMG_3tren)](OTf)\}^+$ and $[Fe^{III}(CN)(TMG_3tren)]^{2+}$, respectively. Figure 3 shows X-band EPR spectra of **3**, recorded in butyronitrile at $T = 2$ and 33 K. The features observed are characteristic of a high-spin ($S = 5/2$) Fe^{III} system with $E/D \approx 0$, where D and E are the axial and rhombic zero-field splitting parameters, respectively. The observed increase in signal intensity (population of the EPR active state) upon raising the temperature from 2 to 33 K indicates that the signal results from an excited state, which implies that $D < 0$.

Crystals of **3** suitable for X-ray analysis were grown at low temperature, and its crystal structure is shown in Figure 1 (Chart 2 and Table 1). Notably, **3** retains the coordination sphere and the strict TBP geometry ($\tau = 1.00$)[39] found for the iron(II) precursor **2**, but displays significantly shortened iron-ligand bond lengths. More specifically, all the Fe−N distances contracted by about 0.09 Å (0.088 and 0.096 Å for $Fe-N_{axial}$ and average $Fe-N_{equatorial}$, respectively), which is fairly typical of oxidation from high-spin iron(II) to high-spin iron(III). The resultant equatorial $Fe-N_{equatorial}$ bond distances are similar to those seen in other high-spin N-donor supported TBP ferric complexes.[17,18,47,48] In contrast, the Fe−CN bond shortens only by about 0.035 Å, which is reflected in a decreased displacement of the iron center away from the equatorial plane defined by the guanidine donors and toward the cyanide ligand (0.431 Å in **2** vs 0.334 Å in **3**). As was the case for **2**, the $Fe-N_{axial}$ bond length in **3** was found to be elongated (nearly 0.2 Å longer than the $Fe-N_{equatorial}$ bonds), which is attributable to the strain inherent in the small bite angles (approximately 80°) of the three conjoined 5-membered chelate rings formed by coordination of TMG_3tren (see above). As might be expected, the $Fe-C\equiv N$ unit in **2** remained highly linear upon oxidation, with the bond angle seen for **3** (178.22°) being effectively the same as that found for **2** (179.53°). The oxidation did appear to cause a slight contraction of the $C\equiv N$ bond length from 1.150(2) Å in **2** to 1.144(4) Å in **3**, but this decrease is within the uncertainty of the X-ray diffraction data.

Electrochemical Generation of 4. As indicated by the cyclic voltammetric trace in Figure 2, the oxidation of **2** to an oxidation level beyond that of **3** requires very high potentials (>1.5 V vs $Fc^{+/o}$) and would therefore be difficult to achieve using conventional chemical oxidants.[49] In such cases, bulk electrolysis represents a convenient alternative.[46,50] To access species **4**, complex **2** must first be oxidized to **3**, which requires only moderate applied potentials. These transformations can be followed by spectroelectrochemical methods. Consistent with its lack of color, the UV−vis spectrum of **2** has no significant absorption features above 300 nm (Figure 4, Table 2). In contrast, the electronic spectrum of **3**, obtained by the application of a potential of 0.4 V, is dominated by an intense band at 422 nm that presumably arises from a ligand-to-metal charge transfer (LMCT) transition.

Table 2. Spectroscopic Properties of 1 and Selected Iron Cyanide Complexes

Complex	S	$E_{1/2}$ (ΔE)[a] [mV]	λ_{max}, nm (ε_{max}, mM cm^{-1})	$\nu_{C\equiv N}$ [cm^{-1}]	E_0 [eV]	E_{PE}, eV (PE area)[b]	δ [mm s^{-1}]	ΔE_Q [mm s^{-1}]
1[c]	2		400 (8.9) 825 (0.26) 865 (0.25)		7123.2	7113.8 (27)	0.09	−0.29
2	2[d]			2101	7122.3	7112.5 (15)		
3	5/2[e]	−270 (110)	422 (9.0)	2126	7124.4	7114.2 (20)		
4	0	1400 (400)	393 (11.6) 584 (8.8)		7126.8	7112.9 (34)	−0.19(2)[f]	−4.45(3)[f]
6[g]	0	<0		2059			−0.22[i]	3.28[i]
7[h]	1		471 (6.3) 609 (10.1)	2129			−0.18[f]	4.35[f]

[a] Reduction potential of the $Fe^{n+/(n-1)+}$ redox couple, versus the Fc^+/Fc couple. [b] PE = pre-edge. [c] See refs 9 and 12. [d] Established via Evans NMR measurements. [e] Established using EPR spectroscopy, see Figure 3. [f] Measured at 4.2 K. [g] See ref 20. [h] See ref 21. [i] Measured at 180 K.

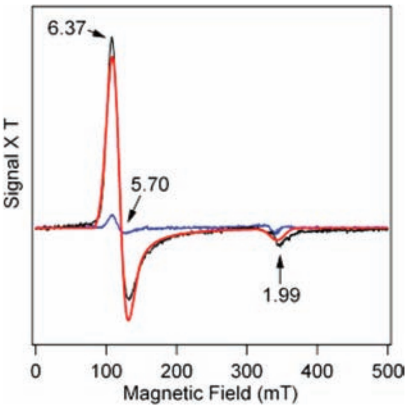

Figure 3. Perpendicular-mode EPR spectra of $[Fe^{III}(CN)(TMG_3tren)]^{2+}$ (**3**) in frozen butyronitrile solution, containing 0.1 M NBu_4BF_4 electrolyte. Spectra were recorded at 2 K (blue curve) and 33 K (black curve). The ordinate, signal × T, is proportional to the population of the excited EPR-active $M_S = \pm 1/2$ state. The red curve is a spectral simulation for an $S = 5/2$ species with zero-field splitting parameters $D = -5.5$ cm^{-1}, $E/D = 0$, and $g_0 = 2.00$ at 33 K, using a packet line width of 10 mT. Conditions: microwave power, 2 mW; microwave frequency, 9.62 GHz; modulation amplitude, 1 mT.

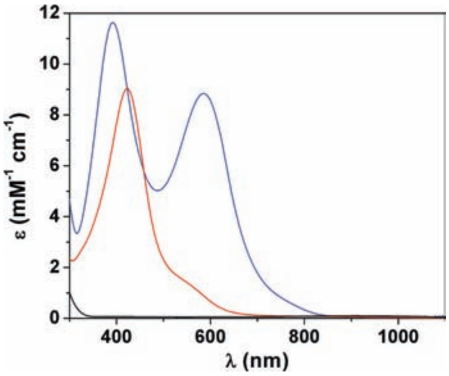

Figure 4. Electronic spectra of **2** (black line), **3** (red line), and **4** (blue line) recorded in CD_3CN solution, containing 0.1 M NBu_4BF_4, at −40 °C.

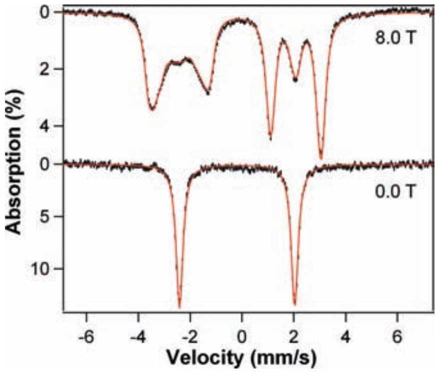

Figure 5. 4.2 K Mössbauer spectra of **4** (black) in acetonitrile recorded in zero and applied magnetic fields as indicated. The red lines are spectral simulations yielding $\delta = -0.19$ mm/s, $\Delta E_Q = -4.45$ mm/s, and $\eta = 0$ (line width 0.31 mm/s, full width at half-maximum).

Further oxidation to **4**, by application of a potential of 2.0 V, leads to replacement of this near-UV LMCT band by two similarly intense bands at 403 and 609 nm. Complex **4** possesses a half-life in CD_3CN solution containing 0.1 M KPF_6 at 25 °C of approximately 15 min, which is about 30 times longer than that of the similarly TMG_3tren-ligated oxoiron(IV) complex **1** ($t_{1/2}$ at 25 °C = 30 s). This disparity can be attributed to the proclivity of the oxoiron(IV) unit to react via facile H-atom abstraction or proton-coupled electron transfer (PCET) pathways.[1,8]

The zero field Mössbauer spectrum of an ^{57}Fe-enriched sample of **4** in frozen acetonitrile solution obtained at 4.2 K exhibits a doublet (representing >95% of Fe) with an isomer shift $\delta = -0.19$ mm/s and a quadrupole splitting $\Delta E_Q = 4.45$ mm/s (Figure 5). The low δ-value, strongly indicative of an iron(IV) oxidation state, and large ΔE_Q are quite similar to those exhibited by the iron(IV) cyanide complexes **6** and **7**, which have respective $S = 0$ and $S = 1$ spin states (see Table 2).[20,21] Simulation of the 8.0 T spectrum reveals that **4** is a diamagnetic species, with $\Delta E_Q < 0$ and $\eta = 0$. The low value of δ and the observation that **4** has a diamagnetic ground state, taken together, show that this complex possesses a low-spin ($S = 0$) Fe^{IV} center. The isomer shift should be contrasted with that of the $S = 2$ oxoiron(IV) complex **1**, which is also supported by the TMG_3tren ligand, but has a significantly larger δ (+0.09 mm s^{-1}) than **4**.

Consistent with its diamagnetic ($S = 0$) ground state, the ^{1}H NMR spectrum of a sample of **4** containing 0.1 M KPF_6,

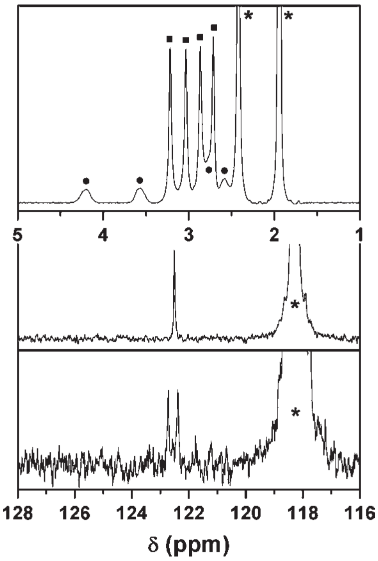

Figure 6. ^{1}H NMR spectrum of 2.5 mM **4** (top panel) recorded at −40 °C in a CD_3CN solution containing 0.1 M KPF_6. Peak assignments: ■ = CH_3; ● = CH_2; * = solvent. ^{13}C NMR spectra of 1 mM **4-^{13}CN** (middle panel) and its ^{57}Fe-labeled isotopomer **4-^{57}Fe(^{13}CN)** (bottom panel) recorded at −40 °C in a CD_3CN solution containing 0.1 M KPF_6. * = solvent. Relaxation time = 5 s.

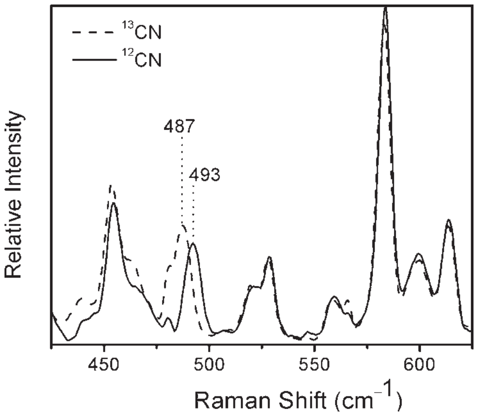

Figure 7. Resonance Raman spectra of $^{12}CN^-$ (solid line) and $^{13}CN^-$ labeled (dashed line) $[Fe^{IV}(TMG_3tren)(CN)]^{3+}$. Spectra were collected using 647.1 nm laser excitation at 60 mW in CD_3CN containing 0.1 mM KPF_6.

recorded at −40 °C exhibits signals with a chemical shift range of 2 to 4.5 ppm (Figure 6, top panel). Although the resonances observed therein are broad and poorly defined, probably because of a combination of (i) the presence of ferric impurities and (ii) high solvent viscosity stemming from the temperature of measurement and high concentration of salts in the sample, it is clear that the C_3-symmetry observed in the ^{1}H NMR spectrum of **2** is retained in **4**. Measurement of the ^{13}C NMR spectrum of **4-^{13}CN**, generated from the ^{13}C-enriched complex **[2-^{13}CN]OTf**, yielded a spectrum with a resonance at 122.5 ppm (Figure 6, middle panel). This peak can be reliably assigned as the cyanide C-atom based on its absence from the spectrum of the natural abundance isotopomer **4** and its similarity to the chemical shift of the CN ligand in **6** (128.9 ppm in C_6D_6 and 131.0 ppm in $CDCl_3$).[20] Furthermore, coordination of the ^{13}CN ligand to the iron center was confirmed by ^{57}Fe-labeling ($I = 1/2$) of **4-^{13}CN**. The resulting ^{13}C NMR spectrum (Figure 6, bottom panel) exhibited a doublet with a small nuclear spin−spin coupling value $^1J(^{13}C{-}^{57}Fe) = 25$ Hz, which reflects the small nuclear g-value of ^{57}Fe ($g_g = 0.18$). Taken together, the Mössbauer and NMR data support the assignment of **4** as an $Fe^{IV}{-}CN$ complex with an $S = 0$ ground state.

Vibrational Spectroscopy. Resonance Raman studies were carried out to probe the origin of the intense UV−vis bands in **3** and **4**. For both complexes, excitation into the intense visible bands led to enhancement of several vibrations that dominate the resonance Raman spectra (Figure 7 and Supporting Information, Figure S6). Notably, excitation at 406.7 nm produces similarly enhanced Raman vibrations in both **3** and **4**, whereas excitation at 647.1 nm into the lower energy LMCT of **4** introduces newly enhanced vibrations. Of these vibrations only one, observed exclusively in the spectrum of **4** at 493 cm^{-1} upon laser excitation into its 609-nm LMCT band, is associated with the cyanide ligand. Its assignment as an Fe−CN vibration is based upon the observed 6 cm^{-1} downshift to 487 cm^{-1} in the ^{13}C-labeled isotopomer **4-^{13}CN** (Figure 7). This shift in energy matches that predicted by Hooke's Law for a diatomic oscillator in which the CN^- ligand is considered as a single body ($\Delta\nu_{theoretical} \approx 6$ cm^{-1}) and is similar in magnitude to those previously observed for ν(Fe−CN) in other iron cyanide complexes.[51−55] The assignment of this vibration as a stretching mode is supported by the absence of any other Fe−CN vibrations. This is indicative of a highly linear Fe−C≡N unit, as seen in the X-ray structures of **2** and **3**, under which circumstances only resonant enhancement of the totally symmetric ν(Fe−CN) would be expected. (Significant resonant enhancement of the bending mode δ(Fe−CN) is only observed upon deviation from linearity.[53,55]) The Fe−CN stretch has nearly constant intensity across the full width of the excitation profile of **4**, while vibrations unperturbed by isotope labeling of the CN ligand in both complexes **3** and **4** exhibit excitation profiles that correlate well with the intensities of observed optical features in both complexes (Supporting Information, Figures S7 and S8). These observations indicate that all the observed LMCT bands originate primarily from the supporting TMG_3tren ligand framework. This conclusion is reinforced by comparison with the solid state off-resonance Raman spectrum of **2** (Supporting Information, Figure S9), which shows many of the same vibrations, albeit slightly shifted in energy relative to those of **3** and **4**. Additionally, the fact that the observed ν(Fe−CN) is not accompanied by the detection of a ν(C≡N) mode corroborates the notion that the optical spectra of **3** and **4** do not arise from a cyanide-to-iron charge transfer transition.

We then turned to IR spectroscopy to characterize the ν(C≡N) modes of these complexes. Cyanide ligands exhibit characteristic stretching vibrations close to 2000 cm^{-1} that are well outside the fingerprint region and hence of great diagnostic use. The ν(C≡N) of 2101 cm^{-1} observed for **2** was found to upshift by 25 cm^{-1} to 2126 cm^{-1}, upon ferrocenium oxidation to **3** (Figure 8). In close agreement with our expectations based upon Hooke's Law for a diatomic harmonic oscillator, which predicts downshifts in these frequencies upon ^{13}C-labeling of approximately 44 cm^{-1}, the ν(C≡N) for **2-^{13}CN** and **3-^{13}CN** were observed at 2056 and 2080 cm^{-1}, respectively. In comparison, the ν(C≡N) of NBu_4CN in acetonitrile solution, which can be thought of as "free" cyanide, was found to be 2052 cm^{-1}. This is at lower energy than seen for metal-bound cyanide, which

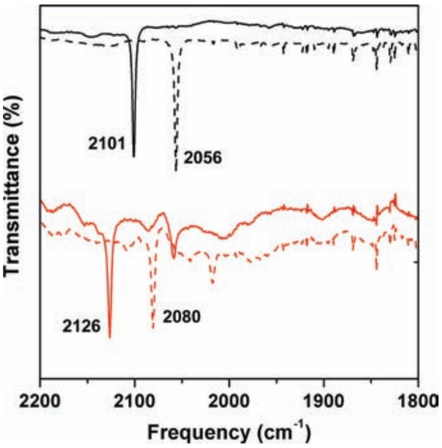

Figure 8. IR spectra of **2** (solid black line), **2-^{13}CN** (dashed black line), **3** (solid red line), and **3-^{13}CN** (dashed red line) recorded in acetonitrile solution at ambient temperatures. The iron(III) complexes were prepared by chemical oxidation, using ferrocenium triflate.

indicates that cyanide bonding to the iron center involves predominant σ-donation from the slightly antibonding σ_5 orbital of cyanide and minimal π-backbonding.[56] Consistent with this notion, the ν(C≡N) of **3** is at higher frequency than that observed for the less Lewis acidic iron center of **2**. A further notable feature of the IR spectrum of **3** is that it contains an additional ^{13}C-sensitive peak at 2059 cm^{-1}, which is in close proximity to the ν(C≡N) seen for NBu_4CN indefinitely and can reasonably be assigned as "free" cyanide. Given that **3** is not indefinitely stable at ambient temperatures, this observation is perhaps unsurprising. Presumably, the greater nuclear charge of the iron(IV) state would lead to an enhanced interaction with the cyanide σ_5 orbital, which would manifest in a further increase in ν(C≡N), but we were unable to obtain an infrared spectrum of **4** because of its thermal instability. The reported IR spectra of the iron(IV) cyanide complexes **6** and **7** provide no insight in this regard because the respective ν(C≡N) of 2059 and 2129 cm^{-1} lack context due to the absence of data for the corresponding ferrous and ferric complexes, which are currently unknown.[20,21]

XANES. The X-ray absorption near edge structure (XANES) spectrum of **2** (Figure 9, Table 2, and Supporting Information, Table S3) possesses split pre-edge features, assigned to 1s → 3d transitions, with a moderately intense peak centered at 7112.5 eV and a weak shoulder at approximately 7114.3 eV (a splitting of 1.8 eV). The integrated pre-edge intensity of 15 for **2** is on the high end of values reported previously for 5-coordinate high spin Fe(II) complexes.[57,58] However, most of these complexes have square pyramidal geometries, and much fewer complexes with TBP sites have been studied. Relevant examples for comparison are the TBP sites in $[Fe^{II}(TPA)(SC_6H_2\text{-}2,4,6\text{-}Me_3)]$ (τ = 0.90) and the $Fe^{II}O_5$ site of the mineral grandidierite, which exhibit pre-edge areas of 8.9[59] and 13 units,[60] respectively. In fact, the latter has a pre-edge spectral pattern similar to that of **2**, with a more intense primary peak and a less intense shoulder that differ by 1.7 eV in energy. The greater intensity of the pre-edge features of **2** relative to other TBP iron sites may reflect an axial distortion imposed by the long apical Fe−N bond from the TMG_3tren ligand. Notably, **2** also exhibits a well-defined shoulder along the rising edge centered at 7118 eV, which must be included in the pre-edge peak analysis to provide a good fit. Similar shoulders have been observed for other cyanoiron(II) complexes such as $K_4[Fe(CN)_6]$ and cyanide-ligated ferrous myoglobin.[57,61] By analogy to those studies, we suggest that this transition is associated with a high-energy combination of the cyanide π^* orbital with metal 3d orbitals, since the energy of this feature is too high to be assigned to a purely metal-centered 1s → 3d transition.[61,62]

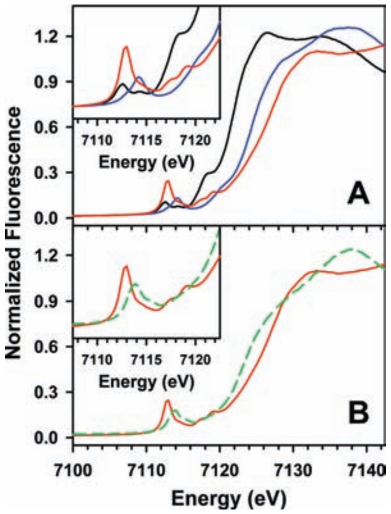

Figure 9. Comparison of Fe K-edge XANES spectra and pre-edge features (insets) of (A) **2** (black line), **3** (blue line), and **4** (red line); (B) **1** (green dashed line) and **4** (red line).

The one-electron oxidation of **2** results in hypsochromic shifts of the edge and pre-edge features by approximately +2 eV (Figure 9, Table 2), consistent with metal-centered oxidation to form a ferric species. In addition, the feature observed on the rising edge of **2** is of much lower intensity in **3**, which is possibly a consequence of a decreased π back-bonding interaction in the latter. The pre-edge region of **3** exhibits a single peak centered at 7114.2 eV with a greater integrated intensity than encountered for **2**, as would be expected from the additional electron hole in **3**. There is also a weak and poorly resolved shoulder on the low-energy side of the primary transition, most likely associated with a small amount of unconverted **2**. Notably, **3** has an integrated pre-edge intensity of 20 units, a value flanked by the 17 units found for the C_{3v} Fe(III) site in yoderite[60] and the 21−27 units reported for Borovik's TBP $[Fe^{III}(H_3buea)(X)]^{2-/-}$ (X = O^{2-}, S^{2-}, HO^{-}) complexes.[63] The higher intensities of the H_3buea complexes may be attributed to the greater deviation of the Fe(III) center out of the equatorial plane in the complexes (0.421, 0.587, and 0.338 Å for X = O^{2-}, S^{2-}, and HO^{-}, respectively,[48,64] vs 0.334 Å for **3**), which would be expected to enhance the probability of 4p orbital mixing into the 3d orbitals.

Electrochemical oxidation of **3** to **4** produces a further hypsochromic shift in edge energy by about +2 eV, from 7124.4 to 7126.8 eV, which is once again indicative of a metal-centered oxidation and by extension formation of an iron(IV) complex. This complex exhibits a relatively sharp pre-edge transition at 7112.9 eV, with a poorly resolved shoulder on its high energy face, which is best modeled using two Gaussians centered at 7112.9 and 7114.5 eV with respective normalized areas of 29.0(8) and 5.1(7). The total area of this pre-edge feature is comparable to that for **1** and published *S* = 1 oxoiron(IV) complexes.[9,34,65] Curiously, the energy of this pre-edge feature is bathochromatically shifted by about −1.5 eV relative to that seen for **3**, suggesting a significant contraction of the d-orbitals upon oxidation. This phenomenon was previously observed by

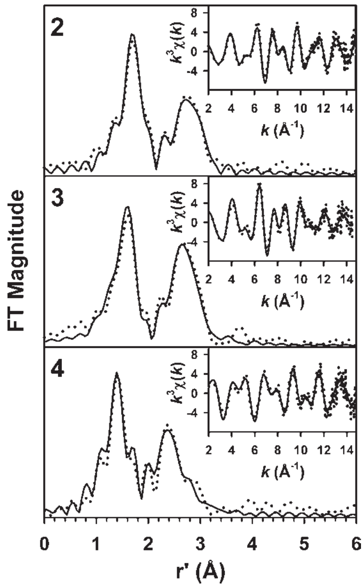

Figure 10. Fits to the Fourier transforms of the Fe K-edge EXAFS data ($k^3\chi(k)$) and unfiltered EXAFS spectra ($k^3\chi(k)$, insets) for **2**, **3**, and **4**. Experimental data is shown with dotted lines, while fits are shown with solid lines. Fourier transformation ranges are as follows: $k = 2.0-14.8$ Å^{-1} (**2**), $k = 2.0-14.5$ Å^{-1} (**3**), $k = 2.0-14.8$ Å^{-1} (**4**). Fit parameters are shown in bold italics in Table 3.

Table 3. EXAFS Analysis of 2, 3, and 4[a]

		Fe−N/C			Fe···C			Fe···C≡N[c]					
species	fit	*n*	*r*	σ^2	*n*	*r*	σ^2	*n*	*r*	σ^2	*F*-factor[b]	*F*′[b]	ΔE_0[b]
2	A	3	2.09	0.8							0.615	2.07	9.39
	B	4	2.09	2.2							0.632	2.31	9.02
	C	3	2.09	0.8	4	3.06	1.9				0.535	1.32	9.19
	D	3	2.09	0.9	6	3.06	3.0				0.384	0.39	9.39
					7	3.42	2.6						
	E	3	2.09	0.6				1	3.27	0.9	0.440	0.61	8.87
	F	3	2.09	0.7	4	3.03	1.4	1	3.28	0.4	0.401	0.47	8.53
	G	***3***	***2.09***	***0.8***	***4***	***3.05***	***2.8***	***1***	***3.28***	***2.0***	***0.340***	***0.28***	***9.36***
					5	***3.42***	***5.0***						
3	A	3	2.02	2.1							0.703	5.02	9.88
	B	4	2.01	3.7							0.703	5.02	9.19
	C	4	2.01	3.7	5	3.00	1.7				0.586	2.74	8.99
	D	4	2.01	3.9	6	3.00	1.9				0.408	0.74	9.38
					8	3.39	2.9						
	E	4	2.01	3.4				1	3.21	1.7	0.550	2.11	8.21
	F	4	2.01	3.8	5	2.98	0.3	1	3.24	0.3	0.455	1.15	8.99
	G	***4***	***2.01***	***3.8***	***5***	***2.99***	***1.6***	***1***	***3.23***	***2.4***	***0.365***	***0.55***	***9.33***
					7	***3.39***	***4.8***						
4	A	4	1.81	3.8							0.723	5.12	1.96
	B	3	1.82	2.1							0.664	3.65	6.76
		1	2.03	1.3									
	C	3	1.83	2.2	6	2.87	2.5				0.485	1.16	8.75
		1	2.04	0.4									
	D	3	1.83	2.2	6	2.86	2.2				0.459	0.93	8.66
		1	2.04	0.3	4	3.46	3.7						
	E	3	1.81	2.4				1	3.04	1.9	0.543	2.09	3.03
		1	2.04	1.5									
	F	3	1.82	2.2	5	2.85	2.3	1	3.08	3.9	0.453	1.18	6.93
		1	2.03	1.2									
	G	***3***	***1.82***	***2.1***	***5***	***2.85***	***2.2***	***1***	***3.08***	***3.5***	***0.425***	***1.09***	***6.62***
		1	***2.03***	***1.3***	***4***	***3.45***	***3.4***						

[a] r is in units of Å; σ^2 is in units of 10^{-3} Å^2. All fits are to unfiltered EXAFS data, as follows: **2**, Fourier transform range of $k = 2.0-14.8$ Å^{-1} (resolution = 0.12 Å); **3**, Fourier transform range of $k = 2.0-14.5$ Å^{-1} (resolution = 0.13 Å); **4**, Fourier transform range of $k = 2.0-14.8$ Å^{-1} (resolution = 0.12 Å). [b] $F\text{-factor} = [\Sigma k^6(\chi_{\text{exptl}} - \chi_{\text{calc}})^2/\Sigma k^6 \chi_{\text{exptl}}{}^2]^{1/2}$. A second goodness-of-fit parameter F' is defined as $F' = F^2/\nu$, where $\nu = N_{\text{IDP}} - N_{\text{VAR}}$. F is defined as $\Sigma(\chi_{\text{exptl}} - \chi_{\text{calc}})^2$, N_{IDP} is the number of independent data points, and N_{VAR} is the number of floated variables in each optimization step. The values of F' shown have been divided by a factor of 10^4 for convenience. F' is a measure of whether an added shell significantly improves the fit. E_0 was defined as follows: **2**, 7122.25 eV; **3**, 7124.40 eV; **4**, 7126.84 eV, and this parameter was allowed to float as a single identical value for all shells (ΔE_0, in units of eV). [c] The cyanide was assumed to be linearly bound, and thus all multiple-scattering paths associated with the Fe−CN moiety were constrained to have identical r and σ^2 parameters.

Wieghardt and co-workers upon oxidation of the $S = 5/2$ iron(III) center in a $[\text{Fe}^{\text{III}}(\mu\text{-O})(\mu\text{-carboxylato})_2\text{M}^{\text{III}}]^{4+}$ (M = Fe, Cr) complex to $S = 1$ iron(IV) and is most likely a consequence of moving from a high-spin to low-spin electronic configuration.[45] In line with this suggestion, complex **1** exhibits a pre-edge feature (7113.8 eV) at higher energy than **4**, but a rising K-edge (7123.2 eV) at lower energy. The latter probably reflects a mitigation of effective nuclear charge associated with the +4 oxidation state by increased covalency associated with the Fe═O unit. Consistent with this notion, the hypsochromic edge-shift of +4.5 eV observed upon oxidation of **2** to **4** is more than twice as large as that seen upon oxidation of **8** to **1** (+2.1 eV).[9] Interestingly, the pre-edge region of **4** also displays two well-defined low-intensity peaks on the rising K-edge that we speculate arise from transitions into the π^* orbitals of the cyanide ligand.

EXAFS. Extended X-ray absorption fine structure (EXAFS) analysis of **4** provides metrical parameters for its iron coordination environment for comparison with crystallographic data on **2** and **3** described in an earlier section as well as EXAFS data on these complexes. The unfiltered $k^3\chi(k)$ EXAFS data and corresponding Fourier transforms for **2**, **3**, and **4** are shown in Figure 10, along with representative best fits. The Fourier transforms for all three species are of similar appearance, but exhibit a progressive shift to smaller r' values as the iron oxidation state increases, consistent with shortening of the metal−ligand bond lengths.

EXAFS curve fitting for **2** revealed a structure consistent with that obtained by X-ray crystallography (see Table 3 for a limited set of fits, and Supporting Information, Tables S4 and S5 for further fitting details). The first coordination sphere can be modeled with 3−4 Fe−N/C scatterers at 2.09 Å, assignable to the equatorial nitrogens of the TMG$_3$tren ligand and the cyanide C atom. The ambiguity in the coordination number for this shell is in line with uncertainties arising from a set of like scatterers having a range of similar Fe-donor atom bond distances. We were unable to refine a longer Fe−N distance that would be associated with the apical nitrogen donor. This effect, which was previously observed in EXAFS studies of **1** and its self-decay product,[9,12] may be a consequence of destructive interference between scattering atoms in the inner shell (Supporting Information,

Figure S12). Although a significant portion of the outer-shell features can be attributed to two shells of Fe$\cdots$C/N scatterers, the quality of the fit to the outer-shell features is improved significantly by the inclusion of multiple-scattering paths from a linearly coordinated cyanide ligand (compare fits **2**-D and **2**-G in Table 3, and also in the Supporting Information, Table S5), the 3.28 Å length of which is essentially identical to that of the crystallographically defined Fe$\cdots$N$_{CN}$ distance of 3.279 Å.

Our EXAFS analysis of scatterers **3** reveals a first coordination sphere consisting of 4 Fe−N/C scatterers at 2.01 Å (fit **3**-A, Table 3), which is comparable to the average of the crystallographically observed Fe−N$_{guanidine}$ and Fe−CN distances (2.034 Å) and can be assigned accordingly. (Because the 0.08 Å difference between the average Fe−N$_{guanidine}$ (2.014 Å) and the Fe−CN (2.094 Å) bond lengths from X-ray crystallography is smaller than the 0.13 Å resolution of the EXAFS data for **3**, these two shells cannot be distinguished by EXAFS.) Notably, the 0.08 Å shortening seen in the first coordination sphere, upon moving from **2** to **3**, is very similar to the change in the average Fe-donor atom distance seen crystallographically (0.082 Å). While the total coordination number is more in line with that expected for a 5-coordinate TBP site compared to **2**, we were once again unable to resolve a long Fe−N$_{axial}$ distance without worsening the fit quality and obtaining implausibly large Debye−Waller factors (Supporting Information, Tables S4 and S6). As with **2**, inclusion of multiple-scattering contributions from a linearly coordinated cyanide ligand significantly improves the quality of the fit (fit **3**-G, Table 3). The shortening in refined r' values obtained for the bound cyanide is again consistent with the increased oxidation state of **3**, with the Fe$\cdots$N$_{CN}$ distance of 3.23 Å being in excellent agreement with that seen in its X-ray structure (3.237 Å).

One-electron oxidation of **3** to **4** engenders profound changes in the iron coordination environment. Specifically, the best fit to the inner shell now consists of 3 Fe−N/C scatterers at 1.82 Å, associated with the equatorial nitrogen donors and the coordinated cyanide by analogy to **2** and **3**, and 1 Fe−N scatterer at 2.03 Å that can be assigned to the Fe−N$_{axial}$ interaction that we were unable to detect via EXAFS analysis in either **2** or **3** (Table 3). The shortening in the former distance by almost 0.2 Å compared to **3** is likely a reflection of both the higher oxidation state of **4** and the conversion from the high-spin $S = 5/2$ state in **3** to the low-spin $S = 0$ spin state of **4**. Indeed, this Fe−N distance of 1.82 Å is comparable to the average Fe−N bond length of 1.773 Å observed in the X-ray structure of the recently reported $[Fe^{IV}(N{=}C^{t}Bu_2)_4]$,[66] which is the only other example of a structurally characterized $S = 0$ iron(IV) complex, with the slightly shorter bond lengths in the latter presumably resulting from its lower coordination number. In addition, the outer-shell features of **4** can be fit with a combination of single-scattering Fe$\cdots$C/N shells from the TMG$_3$tren ligand and multiple-scattering paths associated with a linearly coordinated cyanide, similar to our fits of **2** and **3** (fit **4**-G, Table 3 and Supporting Information, Table S7). In particular, the observed 0.15 Å decrease in the Fe$\cdots$N$_{CN}$ distance to 3.08 Å is of comparable magnitude to the contraction observed in the first coordination sphere.

The influence of spin state is clearly illustrated by comparison of the structural parameters obtained in the EXAFS analysis of **4** to those from the X-ray structure of the similarly TMG$_3$tren-ligated $S = 2$ oxoiron(IV) complex **1**,[12] which was found to have an Fe−N$_{axial}$ and average Fe−N$_{equatorial}$ bond lengths of 2.112(3) and 2.005 Å, respectively. In actuality, these distances more closely agree with the corresponding bond lengths in the high-spin iron(III) complex **3**. The striking differences in bond lengths between **1** and **4** most likely reflect a confluence of several factors, namely, the dicationic charge of complex **1** versus the tricationic charge of **4**, the reduced effective nuclear charge at the iron center of **1** because of the high covalency of the Fe^{IV}=O unit, and the substantial contraction of the d-orbitals in **4** as a consequence of its $S = 0$ spin state.

■ CONCLUSIONS

Herein we have detailed the electrochemical oxidation of the high-spin ($S = 2$) iron(II) cyanide complex **2** to the corresponding iron(IV) complex **4**, via the $S = 5/2$ iron(III) complex **3**. The iron-centered nature of these oxidations was confirmed by the accompanying sequential 2 eV hypsochromic shifts of the edge energy in the Fe K-edge spectra of these complexes, the axial $S = 5/2$ EPR signal associated with **3**, and the negative isomer shift observed in the Mössbauer spectrum of **4**. In contrast to the high-spin $S = 2$ state of the similarly TMG$_3$tren ligated Fe^{IV}=O complex **1**, **4** was found to have a $S = 0$ spin-state, like the other known TBP iron(IV) cyanide complex **6**. The $S = 0$ ground state of **4** is evident in its Mössbauer and NMR spectra, and the large contraction in iron-ligand bond lengths relative to those of **1**. The difference in spin state with the similarly ligated $S = 2$ oxoiron(IV) complex **1** is presumably a consequence of the strong π-donating properties of the oxido ligand, which cyanide does not possess, that destabilize the $\{d_{yz}, d_{xz}\}$ antibonding combinations (occupied by four electrons in **4**) and narrow the energy gap with the equatorial $\{d_{xy}, d_{x^2-y^2}\}$ orbital pair. This manifests in significant spectroscopic changes that can be viewed within the context of the series of iron(II) to (IV) complexes **2**− **4**, in which a TBP ligand framework is maintained.

Complex **4** is of strong interest, with it being only the third iron(IV) cyanide complex that has been reported and a rare example of a TBP iron(IV) complex. In contrast to the previously reported cyanoiron(IV) complexes **6** and **7**,[20,21] which are respectively supported by trianionic and tetraanionic ligands, **4** is supported by a neutral ligand and is in fact the only existing example of a bona fide mononuclear iron(IV) complex with an overall charge of 3+. The high charge is reflected in the accompanying Fe$^{IV/III}$ reduction potential of approximately 1400 mV vs Fc$^+$/Fc, compared to the negative reduction potentials of the oxoiron(IV) complex **5** (−900 mV)[13] and the iron(IV) cyanide complex **6** (<0 mV),[20] both of which were generated by ferrocenium oxidation of the corresponding iron(III) precursors. Complex **4** has one of the highest iron-centered reduction potentials measured thus far. For comparison, complexes with potentials that flank this value are a tetracationic oxo-bridged diiron(IV) complex reported by Wang et al.[46] with an $E_{1/2}$ of +1500 mV vs Fc$^+$/Fc, and a dicationic chloroiron(IV) complex of Me$_3$cyclam-acetate reported by Berry et al.[24] with an $E_{1/2}$ of +1380 mV vs Fc$^+$/Fc. This study highlights the ability of the sterically protecting, highly basic, neutral donors of TMG$_3$tren to stabilize iron(IV) centers and hints at the potential utility of this and related peralkylguanidyl ligands in accessing other high valent chemistry.

■ ASSOCIATED CONTENT

Ⓢ Supporting Information. ^{1}H NMR spectra of **2** and **8**, room temperature cyclic voltammetry trace for **2**, experimentally observed and calculated ESI-MS spectra for **3**, additional resonance Raman spectra and excitation profiles, X-ray crystallographic data for **2** and **3**, and further XAS analysis details. This material is available free of charge via the Internet at http://pubs.acs.org.

■ AUTHOR INFORMATION

Corresponding Author

*E-mail: larryque@umn.edu; emunck@cmu.edu.

■ ACKNOWLEDGMENT

This work was supported by the National Institutes of Health (Grants GM-33162 to L.Q. and EB-001475 to E.M. and a postdoctoral fellowship 5F32ES017390 to M.A.C.). X-ray crystallographic data collection and structure solutions were conducted by Dr. Victor G. Young, Jr. at the X-ray Crystallographic Laboratory, 192 Kolthoff Hall, Department of Chemistry, University of Minnesota. XAS data were collected on beamline 7-3 at the Stanford Synchrotron Radiation Laboratory (SSRL), a national user facility operated by Stanford University on behalf of the U.S. Department of Energy, Office of Basic Energy Sciences. The SSRL Structural Molecular Biology Program is supported by the Department of Energy, Office of Biological and Environmental Research, and by the National Institutes of Health, National Center for Research Resources, Biomedical Technology Program. We thank Drs. Allyson Aranda and Erik Nelson for their excellent technical support of our XAS experiments. We also thank Professor William B. Tolman for the use of the Avatar IR spectrometer.

■ REFERENCES

(1) Krebs, C.; Galonić Fujimori, D.; Walsh, C. T.; Bollinger, J. M., Jr. *Acc. Chem. Res.* **2007**, *40*, 484–492.

(2) Kovaleva, E. G.; Lipscomb, J. D. *Nat. Chem. Biol.* **2008**, *4*, 186–193.

(3) Price, J. C.; Barr, E. W.; Tirupati, B.; Bollinger, J. M., Jr.; Krebs, C. *Biochemistry* **2003**, *42*, 7497–7508.

(4) Hoffart, L. M.; Barr, E. W.; Guyer, R. B.; Bollinger, J. M., Jr.; Krebs, C. *Proc. Natl. Acad. Sci. U.S.A.* **2006**, *103*, 14738–14743.

(5) Eser, B. E.; Barr, E. W.; Frantom, P. A.; Saleh, L.; Bollinger, J. M., Jr.; Krebs, C.; Fitzpatrick, P. F. *J. Am. Chem. Soc.* **2007**, *129*, 11334–11335.

(6) Galonić, D. P.; Barr, E. W.; Walsh, C. T.; Bollinger, J. M., Jr.; Krebs, C. *Nat. Chem. Biol.* **2007**, *3*, 113–116.

(7) Matthews, M. L.; Krest, C. M.; Barr, E. W.; Vaillancourt, F. H.; Walsh, C. T.; Green, M. T.; Krebs, C.; Bollinger, J. M., Jr. *Biochemistry* **2009**, *48*, 4331–4343.

(8) Que, L., Jr. *Acc. Chem. Res.* **2007**, *40*, 493–500.

(9) England, J.; Martinho, M.; Farquhar, E. R.; Frisch, J. R.; Bominaar E. L.; Münck, E.; Que, L., Jr. *Angew. Chem., Int. Ed.* **2009**, *48*, 3622–3626.

(10) Pestovsky, O.; Bakac, A. *J. Am. Chem. Soc.* **2004**, *126*, 13757–13764.

(11) Pestovsky, O.; Stoian, S.; Bominaar, E. L.; Shan, X.; Münck, E.; Que, L., Jr.; Bakac, A. *Angew. Chem., Int. Ed.* **2005**, *44*, 6871–6874.

(12) England, J.; Guo, Y.; Farquhar, E. R.; Young, V. G., Jr.; Münck, E.; Que, L., Jr. *J. Am. Chem. Soc.* **2010**, *132*, 8635–8644.

(13) Lacy, D. C.; Gupta, R.; Stone, K. L.; Greaves, J.; Ziller, J. W.; Hendrich, M. P.; Borovik, A. S. *J. Am. Chem. Soc.* **2010**, *132*, 12188–12190.

(14) Betley, T. A.; Wu, Q.; Van Voorhis, T.; Nocera, D. G. *Inorg. Chem.* **2008**, *47*, 1849–1861.

(15) Parsell, T. H.; Behan, R. K.; Green, M. T.; Hendrich, M. P.; Borovik, A. S. *J. Am. Chem. Soc.* **2006**, *128*, 8728–8729.

(16) Lucas, R. L.; Powell, D. R.; Borovik, A. S. *J. Am. Chem. Soc.* **2005**, *127*, 11596–11597.

(17) MacBeth, C. E.; Golombek, A. P.; Young, V. G., Jr.; Yang, C.; Kuczera, K.; Hendrich, M. P.; Borovik, A. S. *Science* **2000**, *289*, 938–941.

(18) Harman, W. H.; Chang, C. J. *J. Am. Chem. Soc.* **2007**, *129*, 15128–15129.

(19) Mankad, N. P.; Müller, P.; Peters, J. C. *J. Am. Chem. Soc.* **2010**, *132*, 4083–4085.

(20) Cummins, C. C.; Schrock, R. R. *Inorg. Chem.* **1994**, *33*, 395–396.

(21) Bartos, M. J.; Gordon-Wylie, S. W.; Fox, B. G.; James Wright, L.; Weintraub, S. T.; Kauffmann, K. E.; Münck, E.; Kostka, K. L.; Uffelman, E. S.; Rickard, C. E. F.; Noon, K. R.; Collins, T. J. *Coord. Chem. Rev.* **1998**, *174*, 361–390.

(22) Chanda, A.; Popescu, D.-L.; Tiago de Oliveira, F.; Bominaar, E. L.; Ryabov, A. D.; Münck, E.; Collins, T. J. *J. Inorg. Biochem.* **2006**, *100*, 606–619.

(23) Berry, J. F.; Bill, E.; Bothe, E.; Weyhermüller, T.; Wieghardt, K. *J. Am. Chem. Soc.* **2005**, *127*, 11550–11551.

(24) Berry, J. F.; Bill, E.; Bothe, E.; Neese, F.; Wieghardt, K. *J. Am. Chem. Soc.* **2006**, *128*, 13515–13528.

(25) Song, Y.-F.; Berry, J. F.; Bill, E.; Bothe, E.; Weyhermüller, T.; Wieghardt, K. *Inorg. Chem.* **2007**, *46*, 2208–2219.

(26) Adhikari, D.; Mossin, S.; Basuli, F.; Huffman, J. C.; Szilagyi, R. K.; Meyer, K.; Mindiola, D. J. *J. Am. Chem. Soc.* **2008**, *130*, 3676–3682.

(27) Schumann, H. *J. Organomet. Chem.* **1986**, *304*, 341–351.

(28) Blessing, R. H. *Acta Crystallogr., Sect. A: Found. Crystallogr.* **1995**, *A51*, 33–38.

(29) *SAINT+*, V6.45; Bruker Analytical X-Ray Systems: Madison, WI, 2003.

(30) *SHELXTL*, V6.14; Bruker Analytical X-Ray Systems: Madison, WI, 2000.

(31) George, G. N. *EXAFSPAK*; Stanford Synchrotron Radiation Laboratory, Stanford Linear Accelerator Center: Stanford, CA, 2000.

(32) Tenderholt, A.; Hedman, B.; Hodgson, K. O. *AIP Conf. Proc.* **2007**, *882*, 105.

(33) Scarrow, R. C.; Trimitsis, M. G.; Buck, C. P.; Grove, G. N.; Cowling, R. A.; Nelson, M. J. *Biochemistry* **1994**, *33*, 15023–15035.

(34) Rohde, J.-U.; Torelli, S.; Shan, X.; Lim, M. H.; Klinker, E. J.; Kaizer, J.; Chen, K.; Nam, W.; Que, L., Jr. *J. Am. Chem. Soc.* **2004**, *126*, 16750–16761.

(35) Ankudinov, A. L.; Ravel, B.; Rehr, J. J.; Conradson, S. D. *Phys. Rev. B: Condens. Matter Mater. Phys.* **1998**, *58*, 7565–7576.

(36) Riggs-Gelasco, P. J.; Stemmler, T. L.; Penner-Hahn, J. E. *Coord. Chem. Rev.* **1995**, *144*, 245–286.

(37) Naklicki, M. L.; White, C. A.; Plante, L. L.; Evans, C. E. B.; Crutchley, R. J. *Inorg. Chem.* **1998**, *37*, 1880–1885.

(38) Schubert, E. M. *J. Chem. Educ.* **1992**, *69*, 62.

(39) Addison, A. W.; Rao, T. N.; Reedijk, J.; Van Rijn, J.; Verschoor, G. C. *J. Chem. Soc., Dalton Trans.* **1984**, 1349–1356.

(40) Wittmann, H.; Raab, V.; Schorm, A.; Plackmeyer, J.; Sundermeyer, J. *Eur. J. Inorg. Chem.* **2001**, 1937–1948.

(41) Di Vaira, M.; Orioli, P. L. *Acta Crystallogr., Sect. B* **1968**, *24*, 1269–1272.

(42) Britovsek, G. J. P.; England, J.; White, A. J. P. *Inorg. Chem.* **2005**, *44*, 8125–8134.

(43) Zart, M. K.; Sorrell, T. N.; Powell, D.; Borovik, A. S. *Dalton Trans.* **2003**, 1986–1992.

(44) Rowe, J. M.; Hinks, D. G.; Price, D. L.; Susman, S.; Rush, J. J. *J. Chem. Phys.* **1973**, *58*, 2039–2042.

(45) Slep, L. D.; Mijovilovich, A.; Meyer-Klaucke, W.; Weyhermüller, T.; Bill, E.; Bothe, E.; Neese, F.; Wieghardt, K. *J. Am. Chem. Soc.* **2003**, *125*, 15554–15570.

(46) Wang, D.; Farquhar, E. R.; Stubna, A.; Münck, E.; Que, L., Jr. *Nat. Chem.* **2009**, *1*, 145–150.

(47) MacBeth, C. E.; Gupta, R.; Mitchell-Koch, K. R.; Young, V. G., Jr.; Lushington, G. H.; Thompson, W. H.; Hendrich, M. P.; Borovik, A. S. *J. Am. Chem. Soc.* **2004**, *126*, 2556–2567.

(48) Mukherjee, J.; Lucas, R. L.; Zart, M. K.; Powell, D. R.; Day, V. W.; Borovik, A. S. *Inorg. Chem.* **2008**, *47*, 5780–5786.

(49) Connelly, N. G.; Geiger, W. E. *Chem. Rev.* **1996**, *96*, 877–910.

(50) Xue, G.; Wang, D.; De Hont, R.; Fiedler, A. T.; Shan, X.; Munck, E.; Que, L., Jr. *Proc. Natl. Acad. Sci. U. S. A.* **2007**, *104*, 20713–20718.

(51) Sitter, A. J.; Reczek, C. M.; Terner, J. *Biochim. Biophys. Acta, Protein Struct. Mol. Enzymol.* **1985**, *828*, 229–235.

(52) Kim, Y.; Babcock, G. T.; Surerus, K. K.; Fee, J. A.; Dyer, R. B.; Woodruff, W. H.; Oertling, W. A. *Biospectroscopy* **1998**, *4*, 1–15.

(53) Han, S.; Madden, J. F.; Siegel, L. M.; Spiro, T. G. *Biochemistry* **1989**, *28*, 5477–5485.

(54) Boffi, A.; Chiancone, E.; Takahashi, S.; Rousseau, D. L. *Biochemistry* **1997**, *36*, 4505–4509.

(55) Simianu, M. C.; Kincaid, J. R. *J. Am. Chem. Soc.* **1995**, *117*, 4628–4636.

(56) Nakamoto, K. *Infrared and Raman Spectra of Inorganic and Coordination Compounds, Part B: Applications in Coordination, Organometallic, and Bioinorganic Chemistry*, 5th ed.; John Wiley & Sons, Inc.: New York, 1997; pp 105−113.

(57) Westre, T. E.; Kennepohl, P.; DeWitt, J. G.; Hedman, B.; Hodgson, K. O.; Solomon, E. I. *J. Am. Chem. Soc.* **1997**, *119*, 6297–6314.

(58) Randall, C. R.; Shu, L.; Chiou, Y.-M.; Hagen, K. S.; Ito, M.; Kitajima, N.; Lachicotte, R. J.; Zang, Y.; Que, L., Jr. *Inorg. Chem.* **1995**, *34*, 1036–1039.

(59) Zang, Y.; Que, L., Jr. *Inorg. Chem.* **1995**, *34*, 1030–1035.

(60) Wilke, M.; Farges, F.; Petit, P.-E.; Brown, G. E., Jr.; Martin, F. *Am. Mineral.* **2001**, *86*, 714–730.

(61) Saigo, S.; Hashimoto, H.; Shibayama, N.; Nomura, M.; Nagamura, T. *Biochim. Biophys. Acta, Protein Struct. Mol. Enzymol.* **1993**, *1202*, 99–106.

(62) Cartier, C.; Momenteau, M.; Dartyge, E.; Fontaine, A.; Tourillon, G.; Bianconi, A.; Verdaguer, M. *Biochim. Biophys. Acta, Protein Struct. Mol. Enzymol.* **1992**, *1119*, 169–174.

(63) Dey, A.; Hocking, R. K.; Larsen, P.; Borovik, A. S.; Hodgson, K. O.; Hedman, B.; Solomon, E. I. *J. Am. Chem. Soc.* **2006**, *128*, 9825–9833.

(64) Larsen, P. L.; Gupta, R.; Powell, D. R.; Borovik, A. S. *J. Am. Chem. Soc.* **2004**, *126*, 6522–6523.

(65) Jackson, T. A.; Rohde, J.-U.; Seo, M. S.; Sastri, C. V.; DeHont, R.; Stubna, A.; Ohta, T.; Kitagawa, T.; Münck, E.; Nam, W.; Que, L., Jr. *J. Am. Chem. Soc.* **2008**, *130*, 12394–12407.

(66) Lewis, R. A.; Wu, G.; Hayton, T. W. *J. Am. Chem. Soc.* **2010**, *132*, 12814–12816.